Accurate visualization of magnetic field distributions associated with operation of commercial batteries using io-SPRITE.

Konstantin Romanenko [a]*, Philip Kuchel [a], Alexej Jerschow [b]

a. School of Life and Environmental Sciences, University of Sydney, Sydney, NSW 2006

b. Department of Chemistry, New York University, 100 Washington Square East, New York, NY 10003

Abstract

Contemporary lithium batteries pose a serious fire risk and should undergo accurate pre-release diagnostics. Manufacturing defects and deviations from normal performance in these power devices can be detected *in operando* with inside-out MRI. This method detects magnetic field perturbations induced by magnetic and conductive components in the battery. Conventional MRI modalities are prone to severe artefacts and signal loss imposed by strongly magnetic cell components. Single point ramped imaging with T_1 enhancement (SPRITE) enables distortion-free visualization of magnetic field patterns associated with cell's mechanical integrity and state of charge. Wireless detection of electrical current inside commercial cells is demonstrated. Imaging weak magnetic fields associated with charge-discharge events can reveal early signs of the battery malfunction and sheds light on the electro-chemical phenomena occurring in the electrolyte and at electrodes. The new approach is demonstrated to achieve sensitive measurements of the magnetic fields originating from electrical current flow inside the cells and provides a means to differentiate normal from defective devices. A solid-state detection medium is introduced here to achieve sensitive and safe io-SPRITE measurements very close to the surface of a battery. The versatility and robustness of the technique is demonstrated by imaging of operating normal and defective iPhone cells.

1. Introduction

Lithium-ion cells (batteries) are the most wide-spread and promising energy storage means for many sectors, including portable electronic devices and transportation, but safety remains a major concern. While the failure rate is relatively low, and the most common causes have been identified [1], a cell malfunction may lead to fires, explosions with potentially disastrous consequences. Our aim is to establish a battery safety-screening methodology that is rapid, non-destructive and universal, *i.e.*, applicable to a wide variety of power-storage devices.

Nuclear magnetic resonance (NMR) spectroscopy and imaging (MRI) are powerful physical-chemical and biomedical analytical techniques gaining traction in fundamental battery research [2–7]. A method termed inside-out (io-) MRI exploits the sensitivity of a magnetic resonance signal to the magnetic susceptibility distribution within an electrochemical cell [8,9]. Information about the battery's magnetic components, defects, state of charge (SOC), and inherent electrochemical processes is encoded in its surrounding magnetic field (MF). The MFs produced by the direct currents within a battery can also be detected with io-MRI. Examining cells during both the charge and discharge cycle provides further means for discriminating between healthy and potentially dangerous battery states.

The choice of MRI modality is critical for accurate io-MRI diagnostics. Strongly magnetized components are common in modern commercial batteries, so conventional frequency encoding and slice selective MRI techniques [10] suffer from severe image misregistration coupled with low sensitivity, due to background magnetic field gradients (short T_2*) [9,11–15]. Recently these challenges have been overcome with fully phase-encoded rapid signal acquisition [9]. Single point ramped imaging with T_1 enhancement (SPRITE) [16–18] provides a fast visualization of solids, and systems, with strong local magnetism [9,19–23].

Here, io-SPRITE was adapted to advanced battery screening. In combination with a solid-state detection medium, io-SPRITE showed high sensitivity to weak MF perturbations that were induced by charge/discharge currents in a set of commercial batteries. MF distributions were examined for different operational modes, direct current (DC) magnitudes, and SOC. Effects associated with battery short circuiting were also visualized.

2. Experimental

iPhone batteries were purchased on-line (eBay.com). The iPhone-8 cell had a rolled design (capacity 1821 mA h; dimensions 90 × 30 × 3 mm^3). The length of the cells exceeded the axial dimension of the RF resonator, and therefore the top and bottom sections were scanned separately, and the images were later combined to form a complete one.

The solid-state io-MRI detection medium consisted of two plastic half-cylinders prepared from a commercially available polymer suspension Plastisol (The Golden Grub Lure Co). The suspension was brought to 165 ºC and poured into a mould. The later was constructed with a beaker (39 mm internal diameter, i.d.) and a rectangular plate (3 mm thick, 39 wide) placed in the centre of the beaker.

Experiments were carried out using a Bruker Avance instrument equipped with a 9.4 T vertical bore magnet (89 mm), a Mini0.75 triaxial gradient system (0.45 T m^{-1}) and GREAT (1/40) gradient amplifiers. The ^{1}H MRI signal was detected with a 40 mm i.d., bird cage resonator (MiniWB57 probe) at a frequency of 400.11 MHz. The centric-scan SPRITE pulse sequence was programmed in Bruker's ParaVision, version 5.2

Three dimensional (3D) *k*-space acquisition was performed in an interleaved fashion [9,20]; 128 sectoral interleaves with 256 excitations per interleaf, giving rise to a (32 × 32 × 32) *k*-space matrix. The following parameters were used in the pulse sequence: RF-excitation pulse duration (P_α) 4 μs; consequent flip angle (α) = π/40; gradient ramp time (T_{GR}) 1 ms; gradient stabilization time (T_{GS}) 0.9 ms; period between RF pulses (T_R) 2 ms; recovery delay (T_0) 1.2 s; phase encoding times (T_P) were in the range from 90 to 130 μs; number of complex data points per excitation, 8; sampling period (*DW*) 5 μs; number of signal averages (*NA*) 1. The total measurement time was 3.8 min.

Image reconstruction and data analysis were performed in Matlab (R2018b, The MathWorks, Inc., Natick, MA). Eight 3D phase images each corresponding to a different phase encoding time (T_P), were extracted from one SPRITE acquisition. The field-of-views (FOV) were scaled using a chirp Z-transform algorithm (11). Local values of magnetic field perturbation were calculated by linear regression of the temporal phase $\varphi(T_P)$ evolution:

$$\Delta B_0(R) = \gamma^{-1} \, d\varphi / dT_P \qquad (1)$$

Phase wrapping was corrected with a custom phase unwrapping approach.

3. Results and discussion

The concept of io-MRI diagnostics relies on accurate mapping of MF variations that are induced by magnetic electrode components, and DC loops. Any deviation of the MF from a standard/control pattern would be interpreted as heralding battery malfunctions. It transpires that the most significant, and therefore the most informative, MF field perturbations occur on the battery surface. Hence, it is important to devise a suitable imaging system.

The original io-MRI battery holder [8] has as a three-compartment cylinder with the middle compartment occupied by the battery. The other two compartments contain water that is doped with $CuSO_4$ to shorten T_1. One of the drawbacks of this setup is the finite thickness of the plastic-polymer compartment walls (~ 2 mm) that protect the battery from the contact with the water. Importantly, the ^{1}H MRI signal from this plastic (acrylonitrile butadiene styrene; ABS) is very weak and does not interfere with the main image. Other potential issues associated with the original design are water leakage, air bubbles, and thermally-induced convection. All these problems can be obviated by constructing a solid detection medium using a soft polymer material such as Plastisol. The contact of the cell with this medium readily enabled visualization of MF field perturbations in it, directly at the surface of the cell. Plastisol's relaxation time constants and high proton content are highly favourable for centric-scan SPRITE images [17,18]. A short T_1 (~ 70 ms) is beneficial for image resolution; and T_2* (~ 2 ms) is long compared with the SPRITE phase encoding interval (T_P ~ 0.1 ms) that ensures T_2* weighting and overall signal attenuation are insignificant influences on image quality.

The use of solid-state detection medium resulted in approximately a four-fold increase in the maximum detectable MF perturbation. An io-SPRITE image of the fully charged iPhone-8 battery is shown in Fig. 1. A schematic of the battery, with the orientations of the imaged regions of interest (ROIs) with respect to the battery, are indicated on the left of the figure. MF perturbations ≈ 100 ppm occurred as a result of an extended nickel tab of the electrode's current collector and the leads (bottom). The MF gradient induced at the tip of the extended tab is close to 0.4 T m^{-1} which is an order of magnitude higher than imaging gradients achieved in modern MRI scanners. These perturbations, due to high MF gradients that are evident close to the battery surface, were not detected with the compartment-based detection medium that samples the signal at a significantly greater distance [9].

Correlations between io-MRI data and the cathode oxidation state can potentially be employed for routine battery diagnostics. The high sensitivity of solid-state io-SPRITE to SOC is demonstrated in Fig. 2 for an iPhone-8 battery.

Data in the histograms were calculated from a series of 3D io-SPRITE images measured over the SOC range from -1440 to -400 mA h (open-circuit battery). In order to remove MF components that were un-associated with SOC (*e.g.* resulting from magnetic tabs and leads), the fully charged battery (SOC = 0) was used as a reference. Maps of MF perturbation in a representative ROI (X-Z slice) are shown in the insets. In the range from -400 to 0 mA h, the effect of SOC was less pronounced.

Current distributions during charge and discharge, and associated MF perturbations depend on the cell design, SOC, and accumulated defects. The DC-induced magnetic field (DCF) of a current wire circulates about the wire thus creating antisymmetric shifts $\pm B_{DC}$ along the external field B_0 (or Z), Fig. 3 (a, b). Numerical simulations of the DCF's z-component of a model three-layer cell, Fig. 3 (b), showed an antisymmetric pattern that became inverted on inversion of the current direction, Fig. 3 (c) [15]. In other words, DCF is expected to circulate about the line connecting the battery tabs (marked with the * symbol).

The iPhone-4 and iPhone-8 cells were used to illustrate the effects of current magnitude and direction in io-SPRITE experiments. The iPhone-4 and iPhone-8 batteries were used to explore the effects of current magnitude and direction on DCFs. Comparison of these models provided a demonstration of the effect of the cell design. The iPhone-4 cell was smaller and didn't contain extended magnetic tabs, in contrast to iPhone-8.

The ROIs displayed in Fig. 4 (a) and Figs. 5 (a, b) cover the lower halves of these batteries, as shown in Fig. 2 (bottom-right), and they include the effects of magnetic leads and extended tabs. The pure DCF maps were derived by subtracting the MF images of the operating and the open-circuit battery near the same SOC. Note, the change in SOC during the SPRITE acquisition was 27 mA h, which corresponded to ~ 1.5 % of the total capacity of the battery.

DCFs of fully charged cells were antisymmetric with respect to the battery plane (Y-Z plane), Figs. 4 (a) and 5 (a). Switching between the modes of operation caused inversion of the DCF. The DCF distribution varied appreciably with the magnitude of the current and the mode of operation (charging/discharging), Fig. 4(b); charging resulted in broader DCF distributions compared to discharging, Fig. 4 (b).

The impact of the charge state on DCF was insignificant over a wide range of SOCs. However, a sharp change occurred near full discharge, SOC = -1440 mA h, Fig. 5 (b). DCF histograms of the fully charged and discharged iPhone-8 batteries are shown in Fig. 5 (c); note that for a given SOC, charging and discharging (± 400 mA) resulted in similar DCF histograms.

The abrupt DCF change below SOC ≈ -1440 mA h was interpreted as being due to non-uniform Li-depletion of the anode. During discharge, the same number of electrons is provided per unit area of the anode per unit time until the moment of local Li depletion. As the depletion progresses, a redistribution of the current density occurs within the anode-current collector. A dependence of DCF on SOC is indicative of the uniformity of the active material of the electrode. In addition, since the resistivity of conductors depends on the temperature, the DCF distribution reports on local temperature variations.

Diagnostics based on io-MRI images include the MF response to various high-risk scenarios, *e.g.* outside the safe SOC range, outside the safe temperature range, after being mechanically damaged, or after being short circuited. Thus, we demonstrated the effect of battery short-circuiting on MF distributions under open-circuit and charge-discharge modes. It was evident that DCF was a sensitive indicator of the local current density that is associated with the extent of homogeneity of electrode coating, and the distribution of resistance in metallic current collectors. These effects were particularly pronounced near full discharge of the battery.

The iPhone-8 battery was gradually discharged (SOC ~ -1800 mA h) and then short circuited through a copper cable (~ 40 cm long, 3 mm diameter). Below, this scenario is referred to as a short circuit #1 (SC#1). The peak temperature of the battery's surface during the discharge was 30 ºC. One hour later, the remaining voltage was 1.3 V. The cell preserved a significant part of its original capacity. It was gradually re-charged to 1620 mA h and short-circuited second time (SC#2). In the course of the second discharge process, the surface temperature peaked at 60 ºC. The cell's capacity dropped by more than two orders of magnitude (~ 7 mA h) and the remaining voltage was ~ 1.5 mV. Due to a low initial charge, the process SC#1, is expected to be considerably less destructive than SC#2.

The process SC#1 resulted in a significant broadening of the open-circuit MF distribution compared with the original state of the battery. Histograms are shown in Fig. 6 for the intact and damaged batteries at their two different SOCs. The deviation of DCFs of the damaged and intact batteries was also significant as evidenced in Fig. 7.

A series of DCF images of the battery that was affected by the short circuit SC#2 was acquired during continuous charging at +400 mA, Fig. 8 (a). The voltage rose to 4.5 V over 25 min, indicating an increase of internal resistance. The DCF distribution broadened with time but did not exhibit significant overall shift; note, the same reference image was used in forming these DCF maps, since the capacity of the cell was too low to appreciate the differences in SOC, Fig. 8 (b). An important observation is that DCF evolved with time, *e.g.*, near the centre and at the bottom of the image slice, Fig. 8 (a), indicating that local currents were intensified by a factor of ~ 2. These changes can be attributed to local processes that affect the overall internal resistance of the battery and hence led to the voltage increase.

Although DCF is a relatively weak effect of the battery operation (MF perturbations ~ 1 ppm) it is a very sensitive marker of the electrode condition. These measurements became possible as a result of overcoming the challenges associated with strong MF gradients (~ 0.4 T m^{-1}) induced by the magnetic components of the battery. Distribution of current density inside an operating battery depends on multiple factors that have a direct impact on DCF. The common factors, some of which were clearly demonstrated in this work, are chemical state and mechanical integrity of the electrodes, battery life cycle events such as development of solid electrolyte interphase (SEI), formation of dendrites, over-discharging, local overheating (hence increase in resistance) and internal or external loop short circuiting.

4. Conclusions

Magnetic components of modern commercial batteries can exert MF perturbations up to 100 ppm of the applied static field. In combination with a solid-state detection medium (Plastisol), io-SPRITE yielded highly sensitive and quantitative mapping of weak magnetic field perturbations that were associated with the operation of a battery. DCF was confirmed as a unique marker of the quality of the battery's manufacturing and its "health". Li-ion battery safety will be improved through understanding the relationship(s) between DCF distributions and hazardous states of battery components. Specifically, the DCF data analysis as part of io-SPRITE diagnostics can be employed to detect premature performance degradation and the onset of battery failures (e.g. due to dendrite formation and internal shorts). Classification of DCF data acquired for various scenarios with this approach may become important for the general deployment of io-MRI in quality control operations.

Acknowledgements

Funding was provided by US National Science Foundation (CBET 1804723), Mercedes-Benz Research & Development North America, and the Australian Research Council (Discovery Project Grant, DP190100510).

References

[1] C. Hendricks, N. Williard, S. Mathew, M. Pecht, A failure modes, mechanisms, and effects analysis (FMMEA) of lithium-ion batteries, J. Power Sources, 297 (2015) 113−120.

[2] S. Chandrasekar, N.M. Trease, H.J. Chang, L.-S. Du, C.P. Grey, A. Jerschow, Li-7 MRI of Li batteries reveals location of microstructural lithium, Nat. Mater., 11 (2012) 311−315.

[3] M. Deschamps, E. Gilbert, P. Azais, E. Raymundo-Piñero, M. R. Ammar, P. Simon, D. Massiot, F. Béguin, Exploring electrolyte organization in supercapacitor electrodes with solid-state NMR, Nature Mater., 12 (2013) 351–358.

[4] H.J. Chang, A.J. Ilott, N.M. Trease, M. Mohammadi, A. Jerschow, C.P. Grey, Correlating Microstructural Lithium Metal Growth with Electrolyte Salt Depletion in Lithium Batteries Using 7Li MRI, J. Am. Chem. Soc., 137 (2015) 15209−15216.

[5] A.J. Ilott, M. Mohammadi, H.J. Chang, C.P. Grey, A Jerschow, Real-time 3D imaging of microstructure growth in battery cells using indirect MRI, Proc. Natl. Acad. Sci., 113 (2016) 10779−10784.

[6] O. Pecher, J. Carretero-González, K. J. Griffith, C. P. Grey, Materials' Methods: NMR in Battery Research, Chem. Mater. 29 (2017) 213−242.

[7] K. Romanenko, MRI studies of plastic crystals, Annual Reports on NMR Spectroscopy, 91 (2017) 67−114.

[8] A.J. Ilott, M. Mohammadi, C.M. Schauerman, M.J. Ganter, A. Jerschow (2018) Nat. Comm. 9:1776.

[9] K. Romanenko, A. Jerschow, Proc. Natl. Acad. Sci. U.S.A 116 (38) (2019) 18783–18789.

[10] M.A. Bernstein, K.F. King, X.J. Zhou, Handbook of MRI Pulse Sequences, Elsevier, 2004.

[11] J.R. Reichenbach, R. Venkatesan, D.A. Yablonskiy, M.R. Thompson, S. Lai, E.M. Haacke, J. Magn. Reson. Imag. 7 (1997) 266–279.

[12] H. Graf, G. Steidle, P. Martirosian, U.A. Lauer, F. Schick, Med. Phys. 33 (2006)124–127.

[13] M.-J. Lee, S. Kim, S.-A. Lee, H.-T. Song, Y.-M. Huh, D.-H. Kim, S.H. Han, J.-S. Suh, RadioGraphics 27 (2007) 791–803.

[14] M.J. Graves, D.G. Mitchell, J. Magn. Reson. Imag. 38 (2013) 269–287.

[15] M. Mohammadi, E.V. Silletta, A.J. Ilott, A. Jerschow, J. Magn. Reson. 309 (2019) 106601.

[16] B.J. Balcom, R.P. Macgregor, S.D. Beyea, D.P. Green, R.L. Armstrong, T.W. Bremner, J Magn. Reson. A 123 (1996) 131–134.

[17] I.V. Mastikhin, B.J. Balcom, P.J. Prado, C.B. Kennedy, J. Magn. Reson. 136 (1999) 159–168.

[18] M. Halse, J. Rioux, S. Romanzetti, J. Kaffanke, B. MacMillan, I. Mastikhin, N.J. Shah, E. Aubanel, and B.J. Balcom, J. Magn. Reson. 169 (2004) 102–117.

[19] K. Romanenko, B.J. Balcom, AIChE J. 58 (2012) 3916–3926.

[20] K. Romanenko, M. Forsyth, L.A O'Dell, J. Magn. Reson. 248 (2014) 96–104.

[21] K. Romanenko, L. Jin, L.A. Madsen, J.M. Pringle, L.A O'Dell, M. Forsyth, J. Am. Chem. Soc. 136 (2014) 15638–15645.

[22] K. Romanenko, J.M. Pringle, L.A. O'Dell, M. Forsyth, Phys. Chem. Chem. Phys. 17 (2015) 18991–9000.

[23] K. Romanenko, L. Jin, P. Howlett, M. Forsyth, Chem. Mater. 28 (2016) 2844–2851.

Figure 1. Left: A schematic of the iPhone-8 battery, {X-Z} and {Y-Z} views, with the current collector and leads shown in red. Right: {X-Z} and {Y-Z} slices through the 3D io-SPRITE image of the iPhone-8 battery, ROIs: 39 × 39 mm. Reference image: Plastisol detection medium.

Figure 2. Histograms of MF distribution induced by the iPhone-8 battery at SOCs in the range from 0 to -1440 mA h (left to right). The inserts show {X-Z} slices through corresponding 3D io-SPRITE maps. The slice location with respect to the battery is indicated in the lower right corner. The current collector and the leads are shown in red. Reference image: fully charged cell (open circuit). [** need to indicate which histogramm is which (it is not obvious) **]

Figure 3. (a) Z - components (± B_{DC}) of circulating magnetic field induced by a current wire. (b) A model of the three-electrode battery. (c) Finite Element simulations, COMSOL Multiphysics (adapted from ref. [15] with permission). The location of tabs is indicated by the "*" symbol.

Figure 4. (a) Longitudinal {X-Z} slices through 3D DCF maps of the operating iPhone-4 battery (± 400 mA) at SOC = 0 mAh (charged). Reference image: fully charged cell (open circuit). (b) Histograms of DCF distributions of the battery operating at ±50, ±100, ±200 and ±400 mA. Standard deviations, σ, shown on the right are grouped by the operation mode (squares - charging, circles - discharging). [** overlapped histograms not visible **]

Figure 5. Longitudinal {X-Z} slices through 3D DCF maps of the operating iPhone-8 battery (± 400 mA) at (a) SOC = 0 mAh (charged) and (b) SOC = -1440 mA h. (c) DCF distributions of the operating iPhone-8 battery. Reference images: intact cell (open circuit) at given SOCs.

Figure 6. MF distributions of the intact and damaged (SC#1) iPhone-8 cells. Reference image: a fully charged intact cell.

Figure 7. Longitudinal slices {X-Z} through the 3D DCF maps of the operating damaged (SC#1) iPhone-8 cell (I = ± 400 mA) at (a) SOC = 0 mAh and (b) SOC = -1620 mA h. (c) DCF histograms of the operating damaged (SC#1) iPhone-8 cell (I = ± 400 mA) at SOC = 0 mA h (re-charged) and SOC = -1620 mA h. Reference images: damaged cell (open circuit) at given SOCs.

Figure 8. Longitudinal slices {X-Z} through 3D DCF maps of the operating damaged (SC#2) iPhone-8 cell (I = + 400 mA). Reference image: damaged cell (open circuit). DCF histograms are shown at 2nd, 10th and 22nd minutes of the continuous charging.

Y-Z

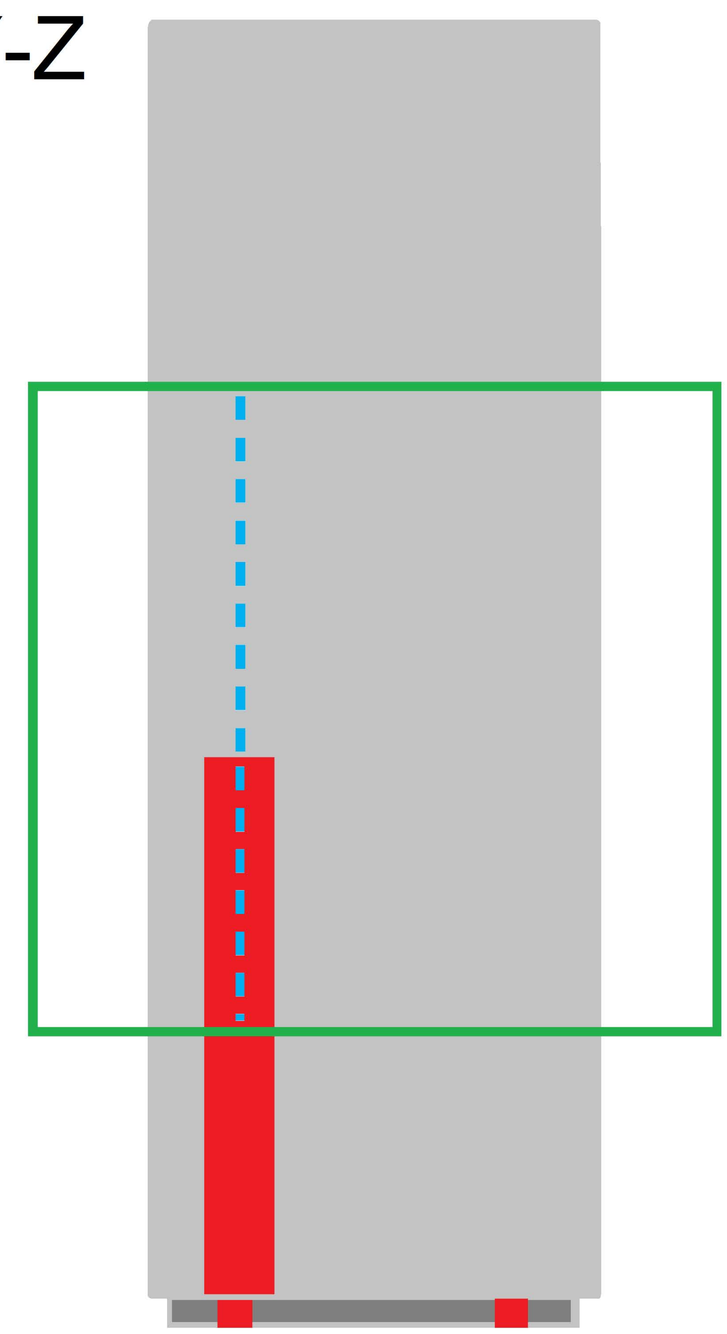

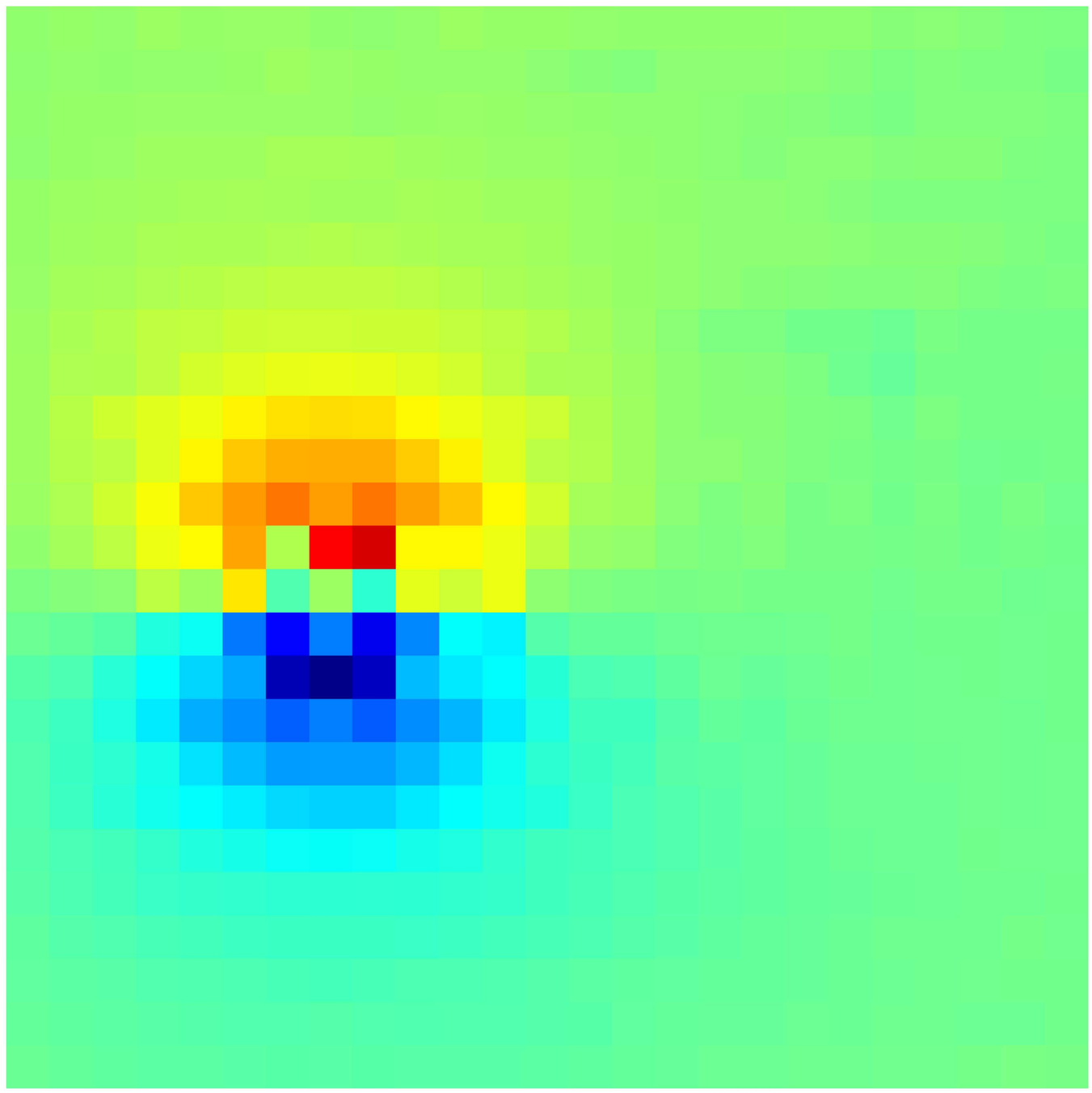

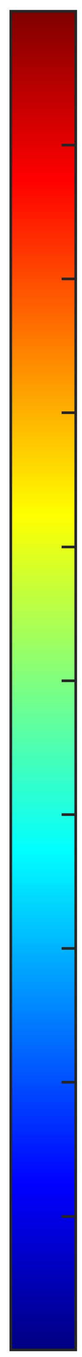

X-Z

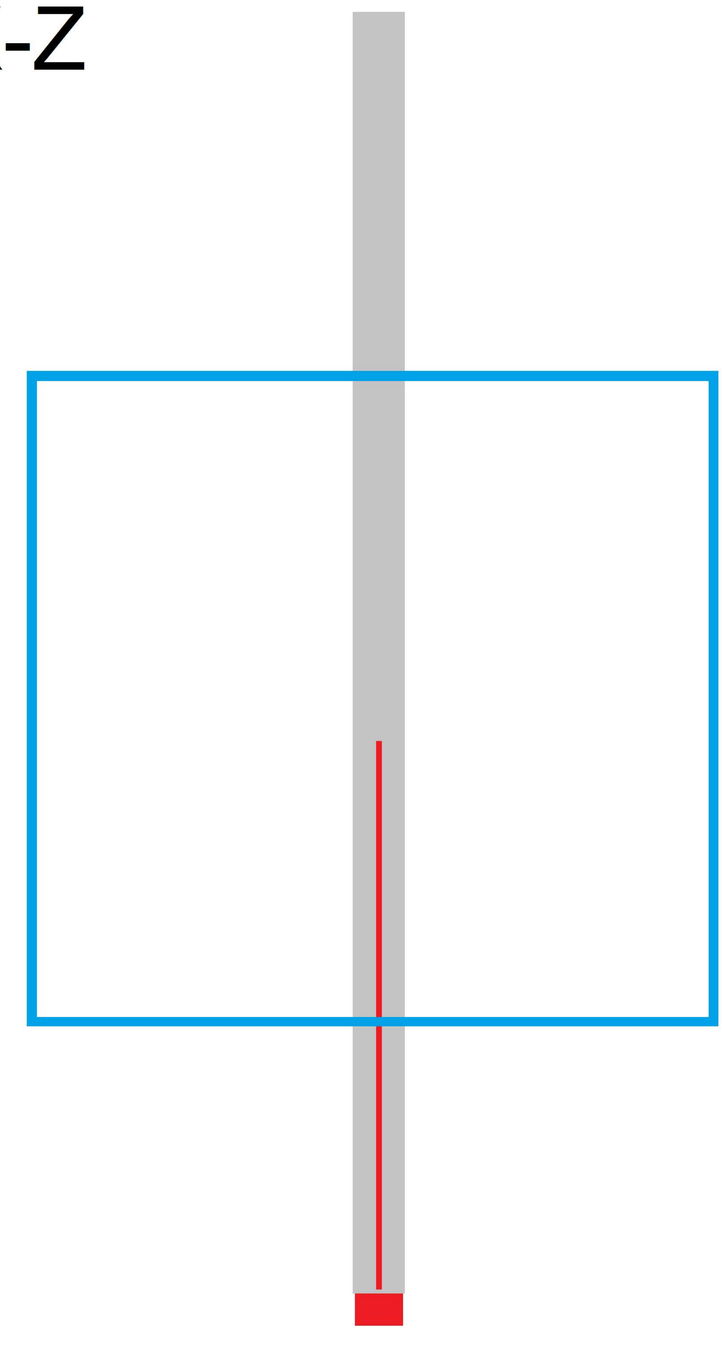

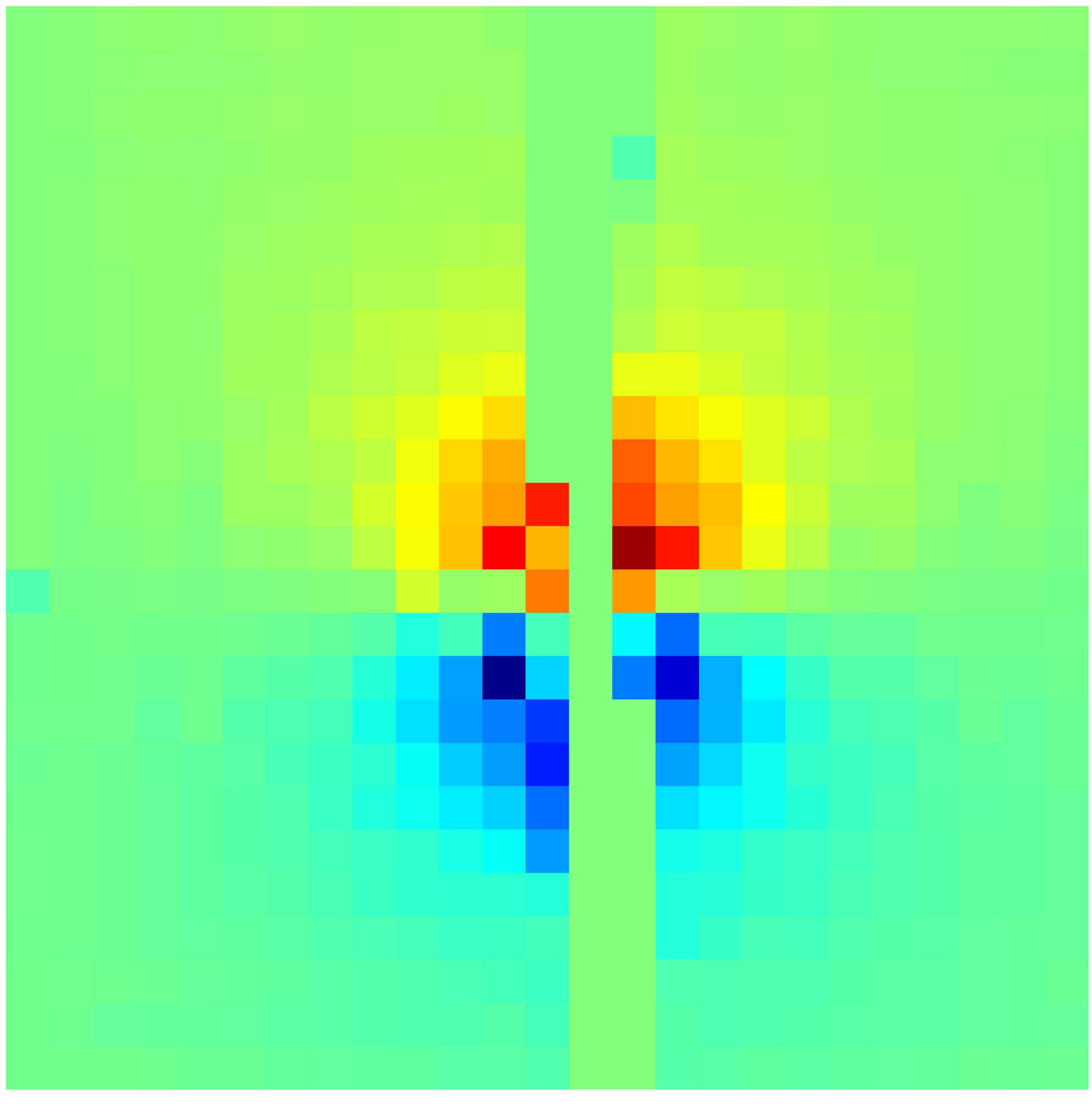

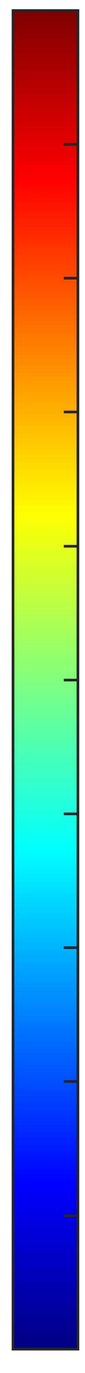

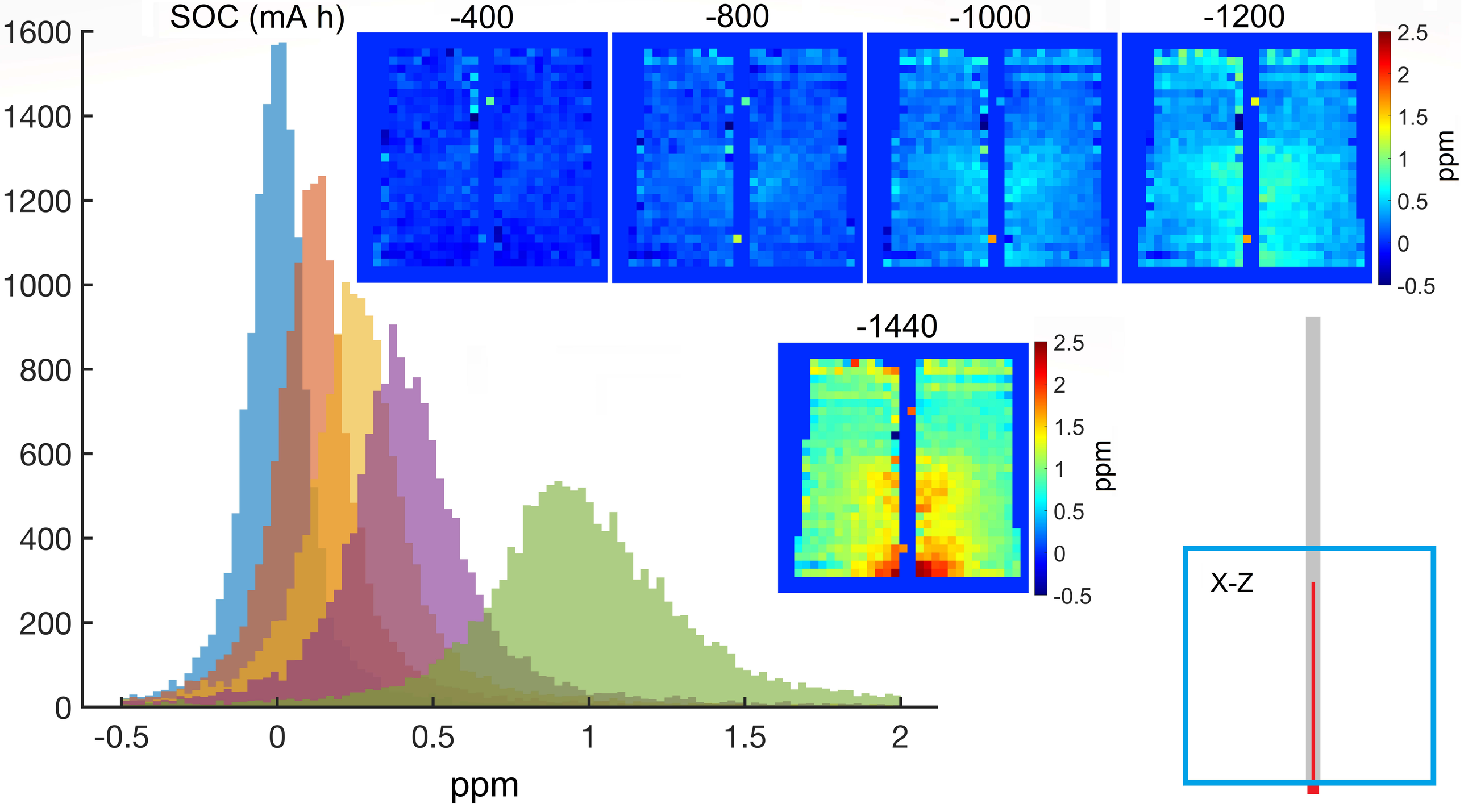
SOC (mA h)
1600
1400
1200
1000
800
600
400
200
0
-0.5
0
0.5
1
1.5
2
ppm
-400
-800
-1000
-1200
2.5
2
1.5
1
0.5
0
-0.5
ppm
-1440
2.5
2
1.5
1
0.5
0
-0.5
ppm
X-Z

a

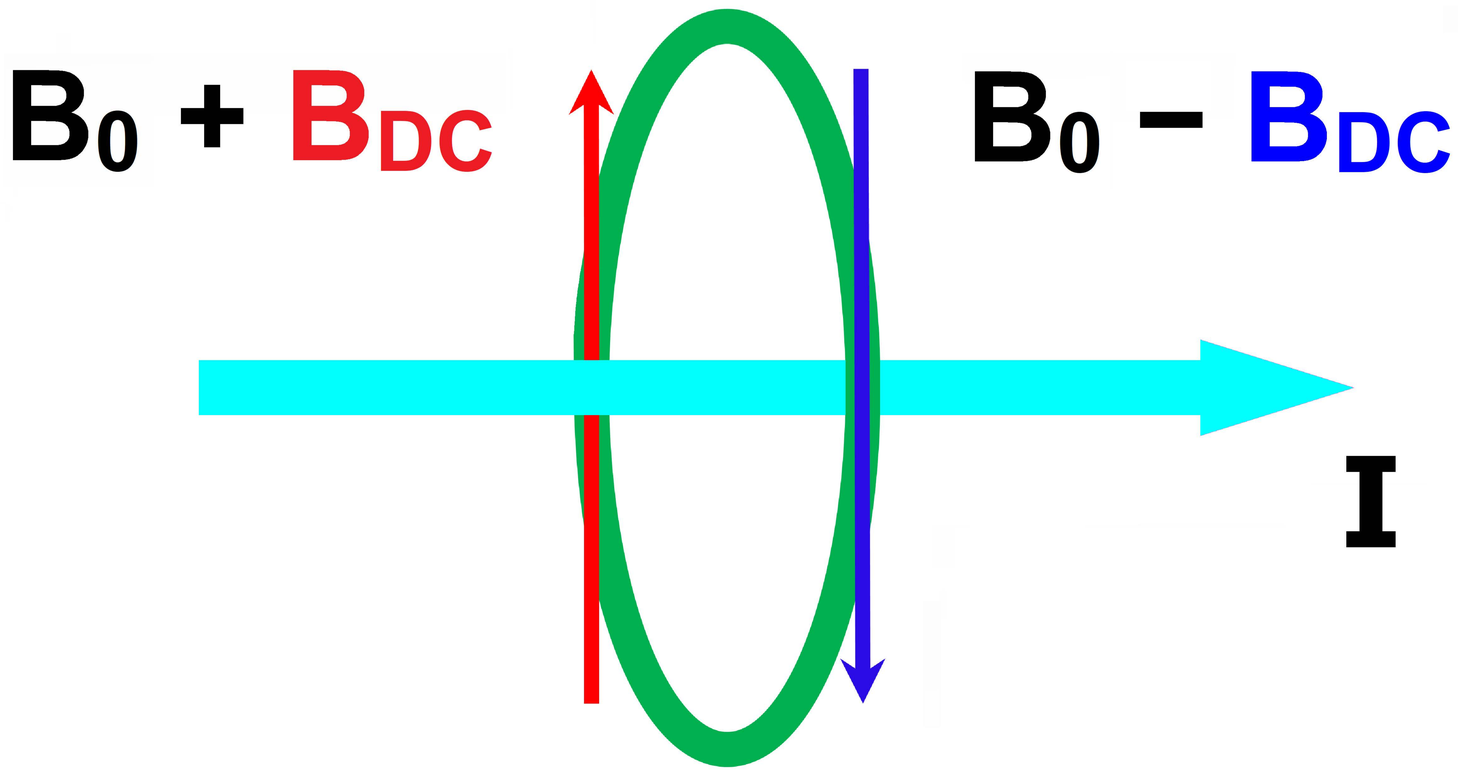

b

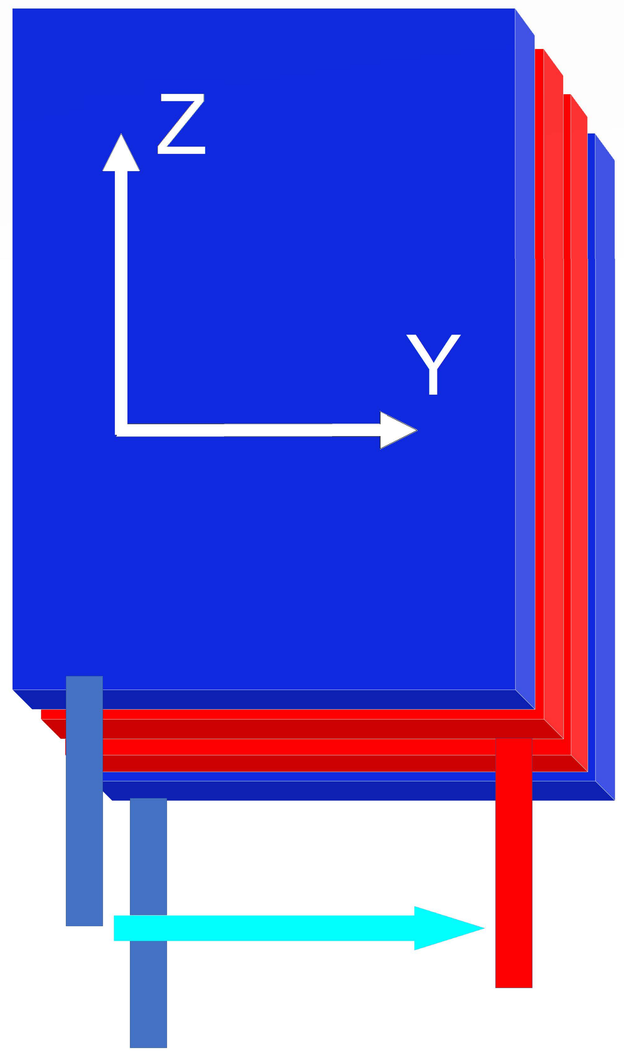

c

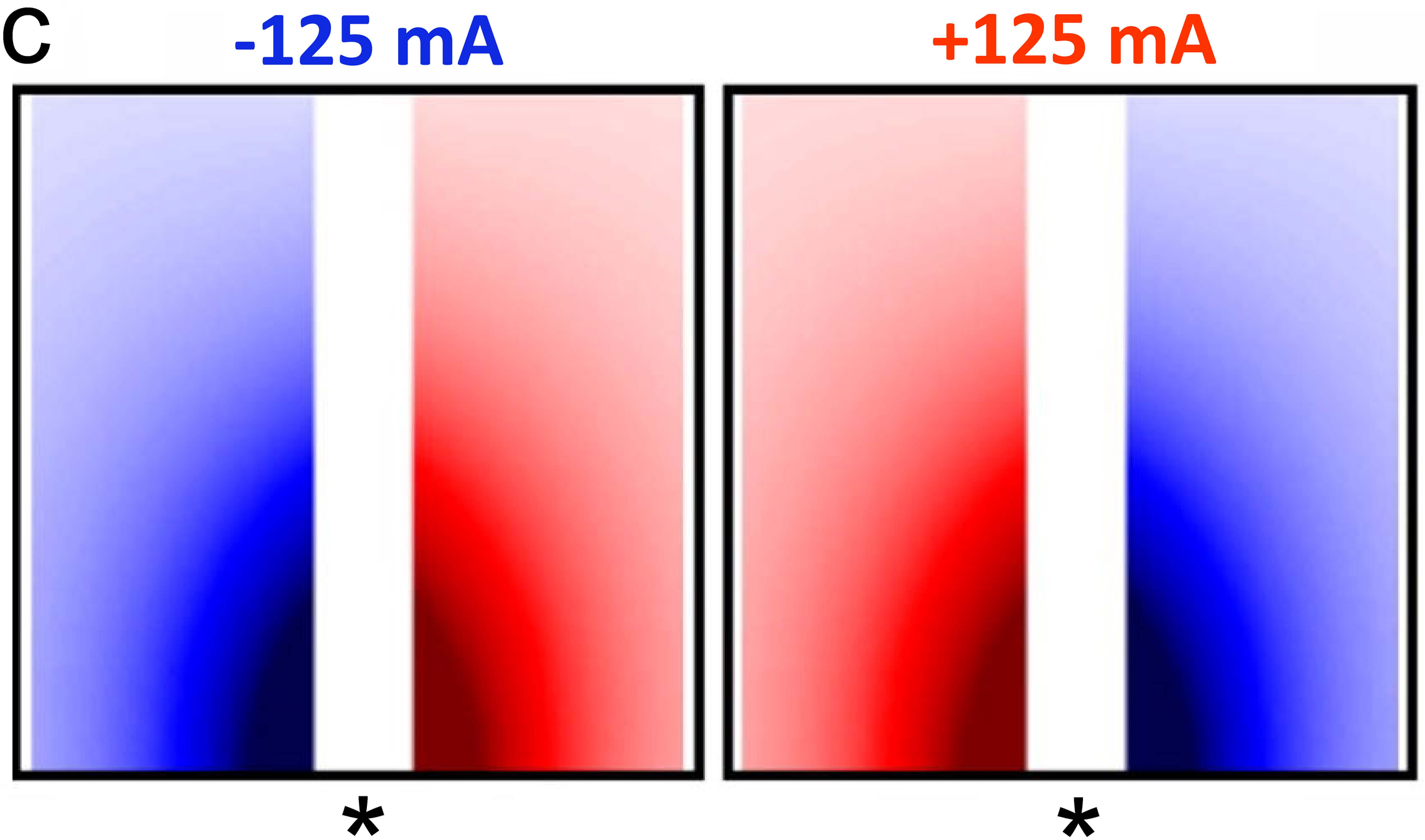

a

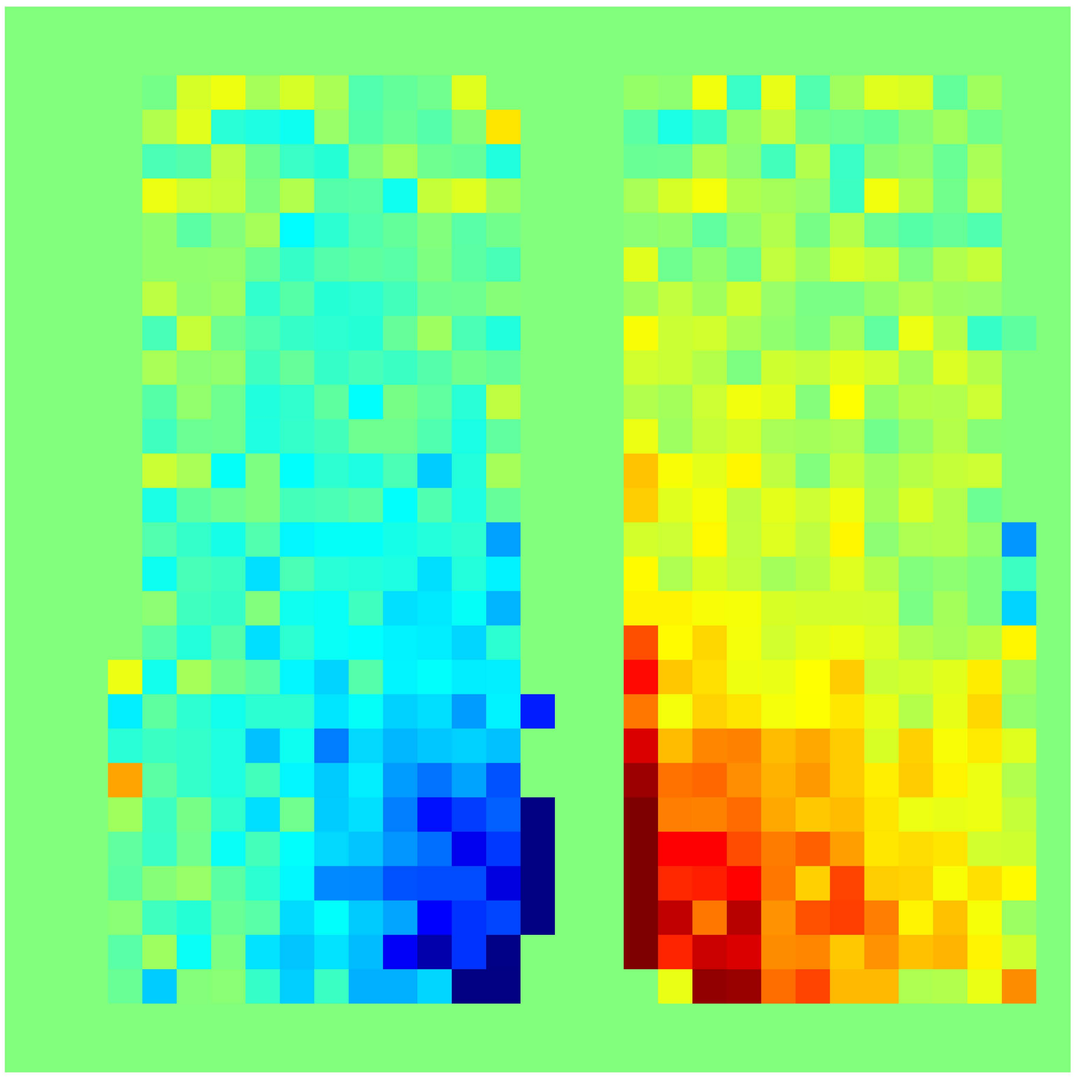
-400 mA

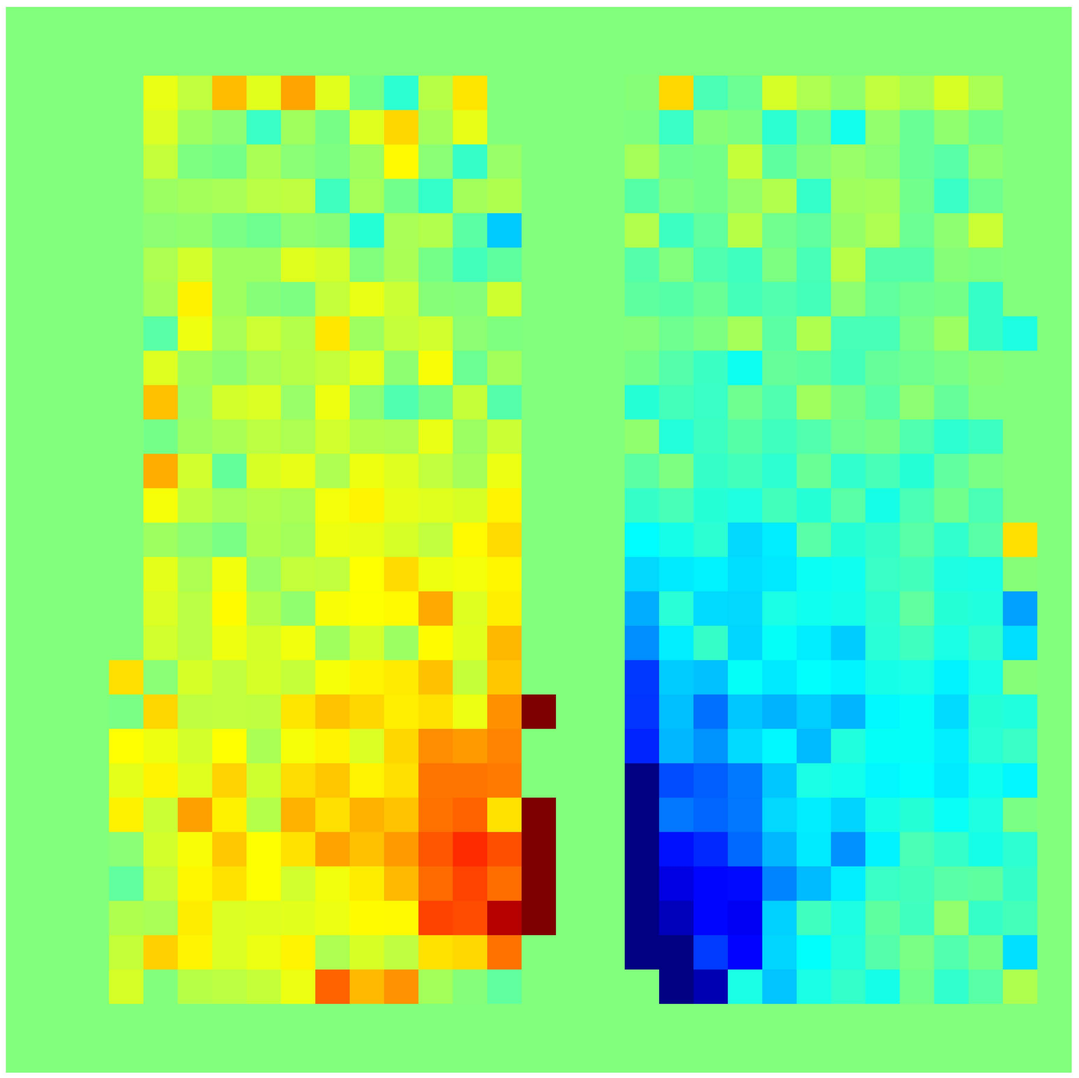
+400 mA

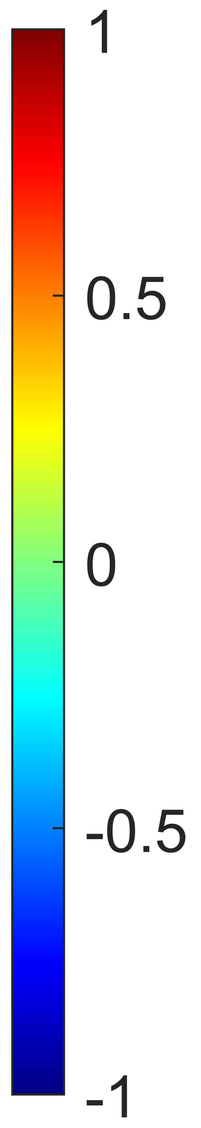
1
0.5
0
-0.5
-1
ppm

b

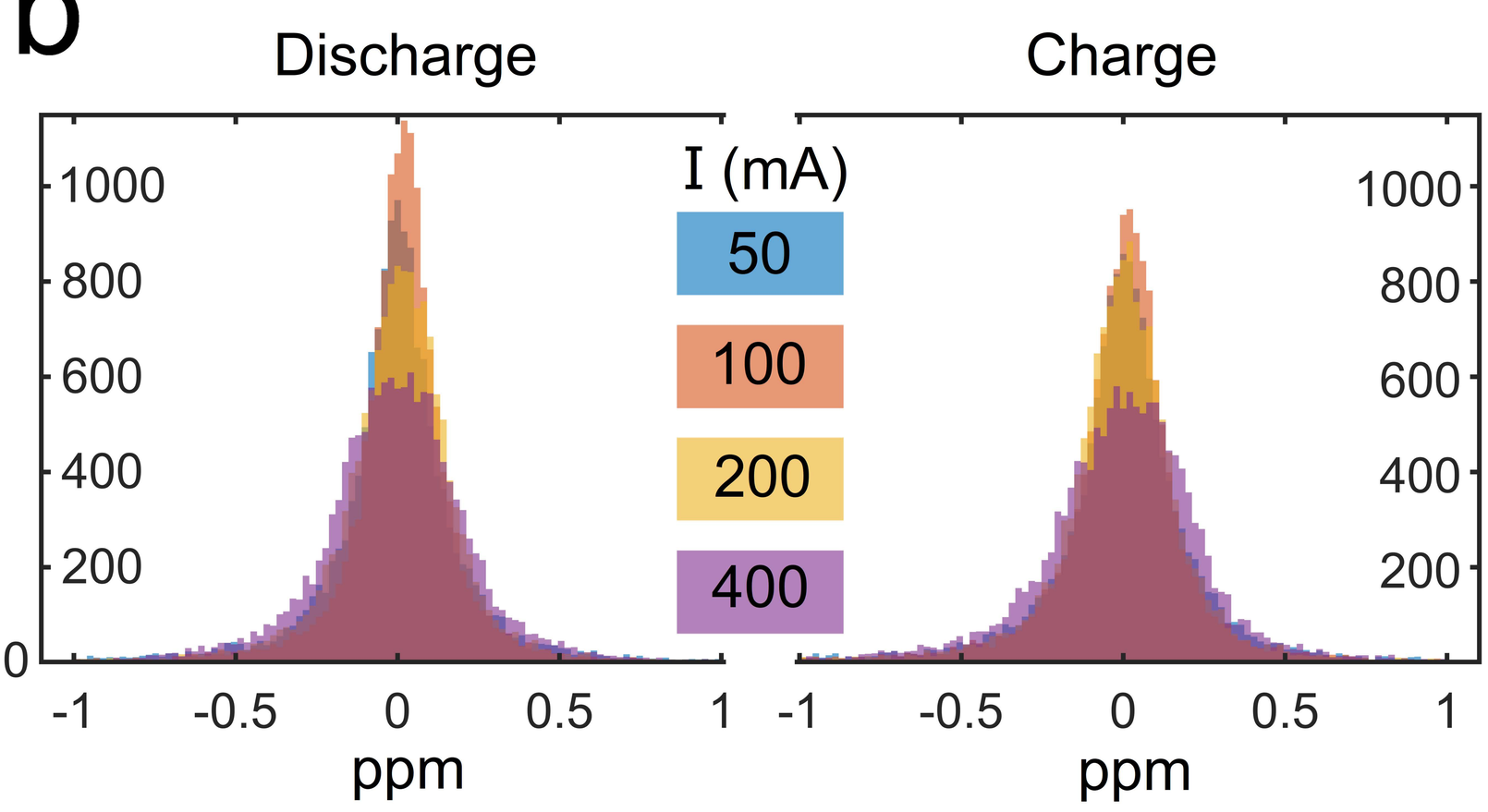
Discharge
Charge
I (mA)
50
100
200
400
1000
800
600
400
200
0
-1
-0.5
0
0.5
1
ppm

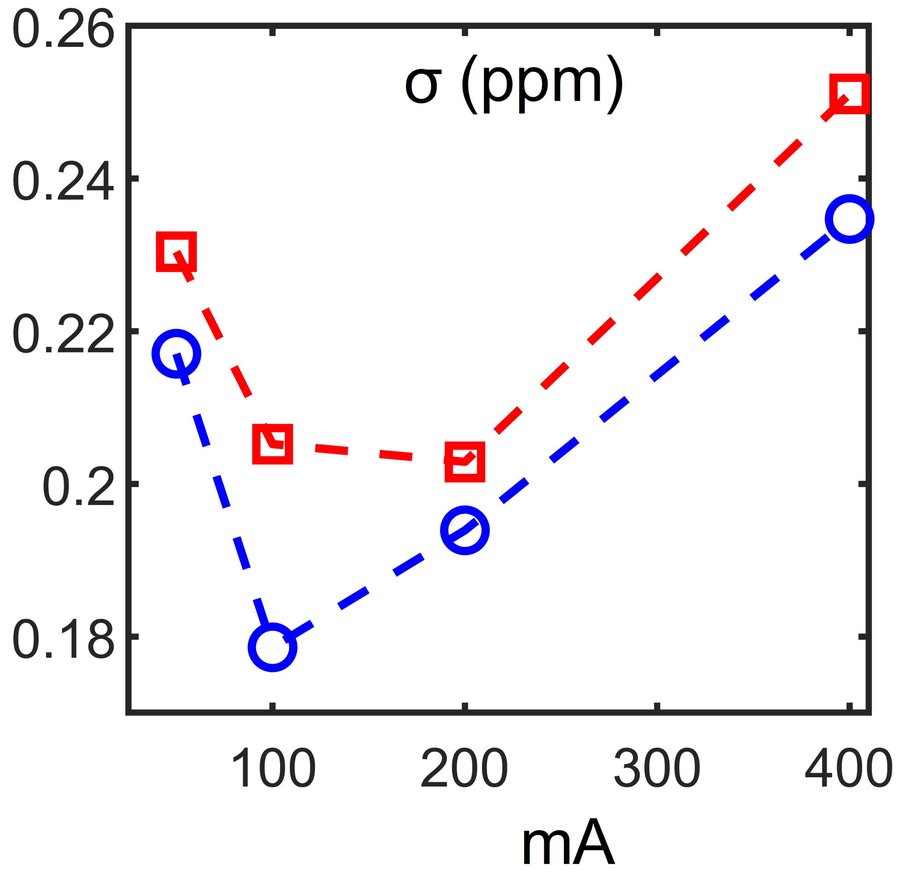
σ (ppm)
0.26
0.24
0.22
0.2
0.18
100
200
300
400
mA

SOC (mA h)

-400

-1440

-1620 *

0 *

2000

1500

1000

500

0

-2

-1

0

1

2

3

ppm

a

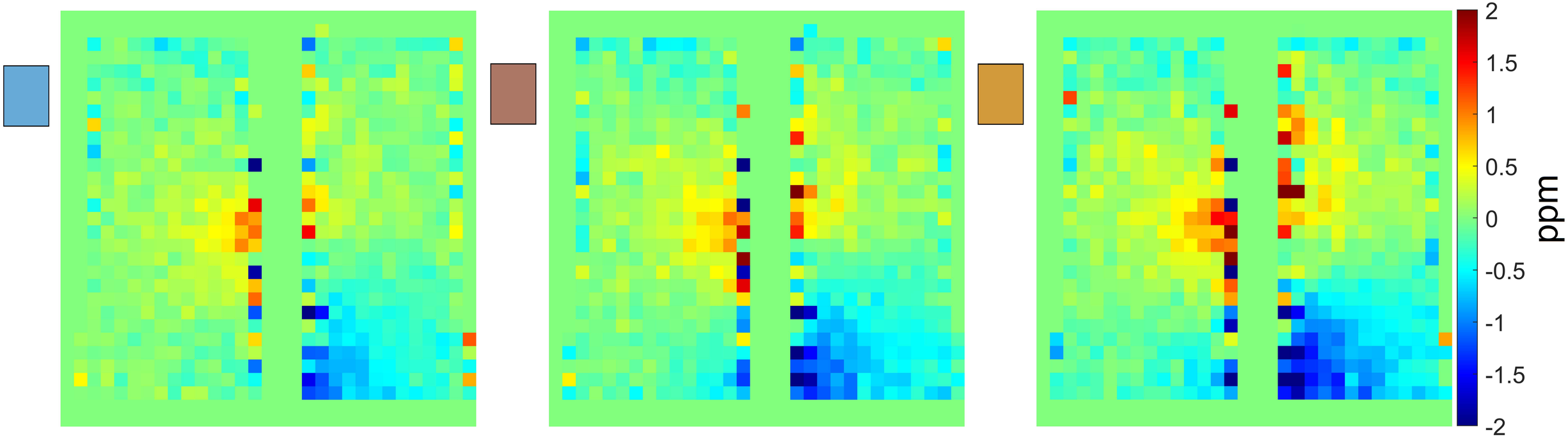
2
1.5
1
0.5
0
-0.5
-1
-1.5
-2
ppm

b

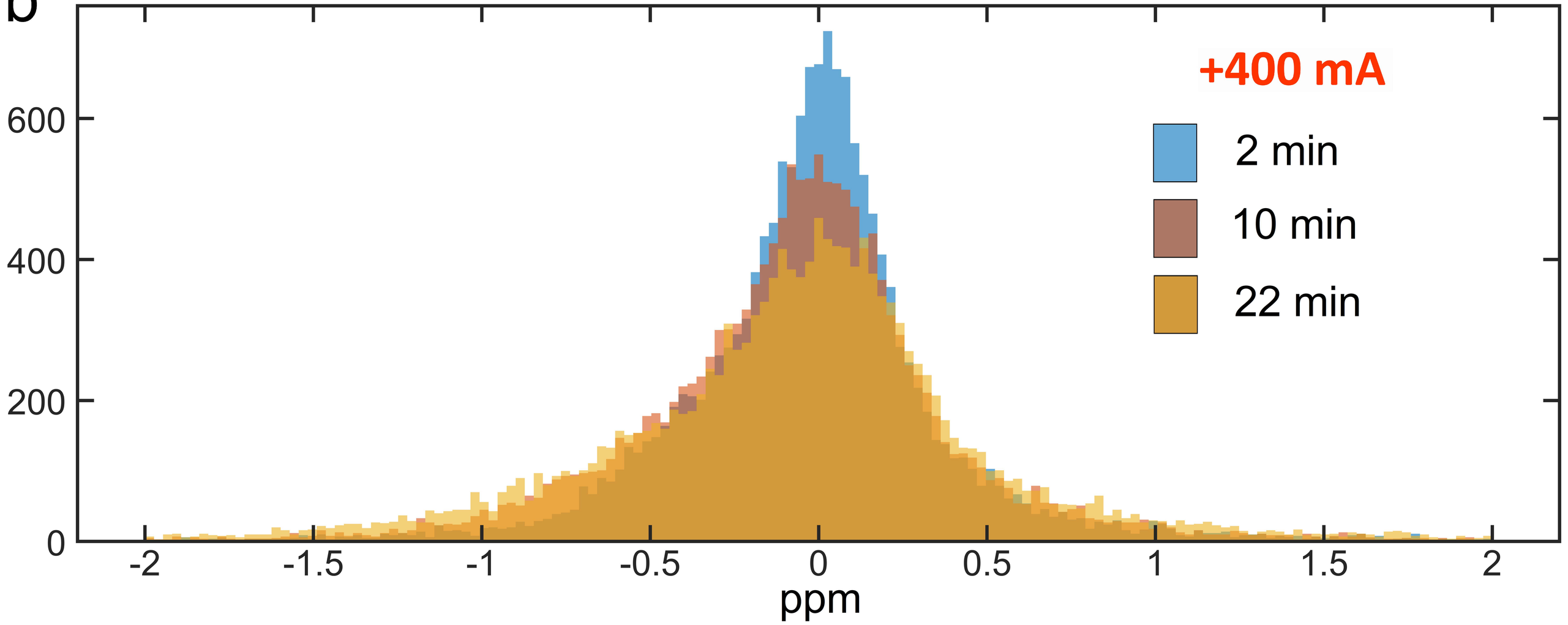
+400 mA
2 min
10 min
22 min
600
400
200
0
-2
-1.5
-1
-0.5
0
0.5
1
1.5
2
ppm

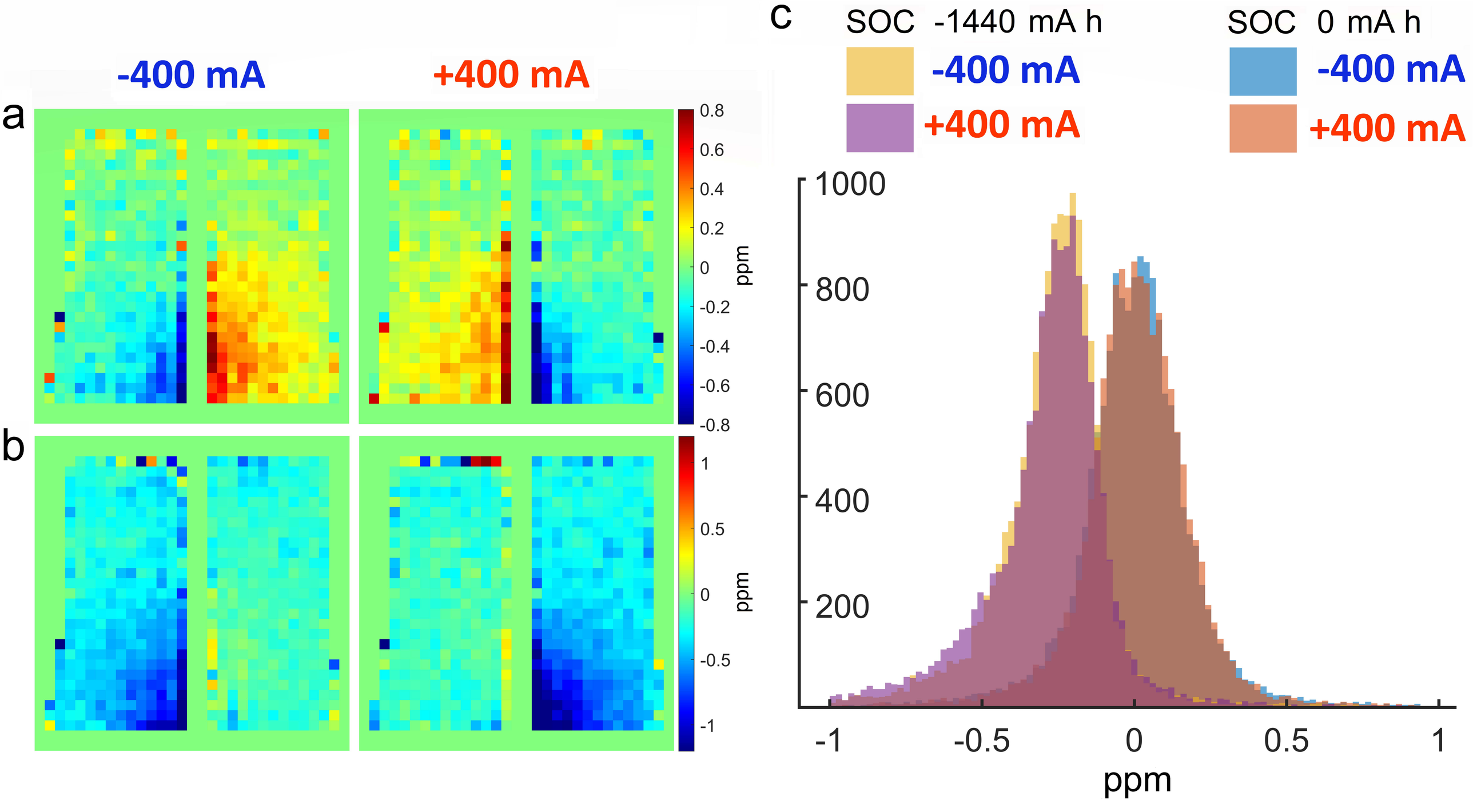
-400 mA
+400 mA
a
b
0.8
0.6
0.4
0.2
0
-0.2
-0.4
-0.6
-0.8
ppm
1
0.5
0
-0.5
-1
ppm
c
SOC -1440 mA h
-400 mA
+400 mA
SOC 0 mA h
-400 mA
+400 mA
1000
800
600
400
200
-1
-0.5
0
0.5
1
ppm

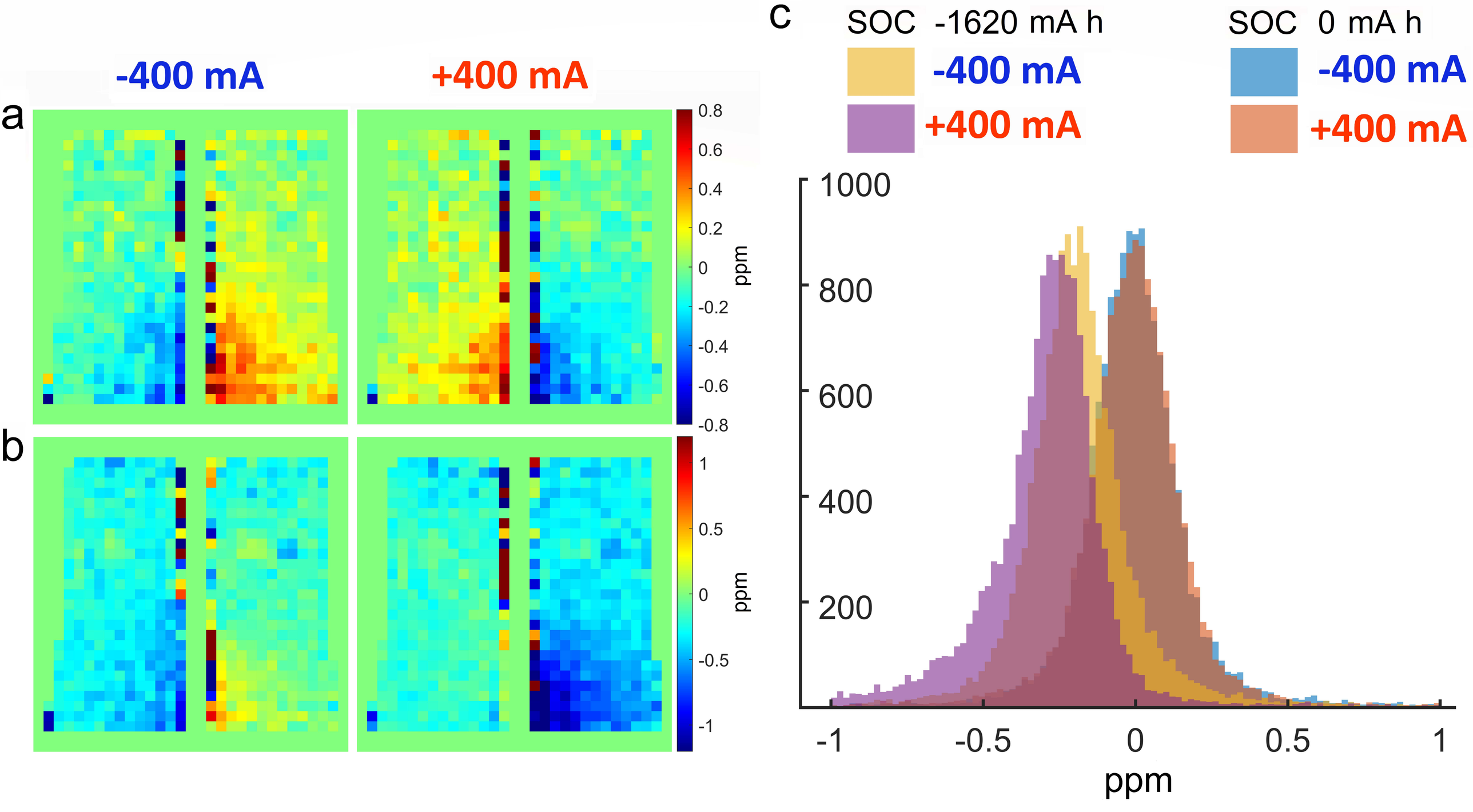
-400 mA
+400 mA
a
b
0.8
0.6
0.4
0.2
0
-0.2
-0.4
-0.6
-0.8
ppm
1
0.5
0
-0.5
-1
ppm
c
SOC -1620 mA h
-400 mA
+400 mA
SOC 0 mA h
-400 mA
+400 mA
1000
800
600
400
200
-1
-0.5
0
0.5
1
ppm